Downloaded from http://rsif.royalsocietypublishing.org/ on December 19, 2017

M: Cucchiara

INTERFACE

rsif.royalsocietypublishing.org

Research

Cite this article: Kim J-K, Varenberg M. 2017 Biomimetic wall-shaped adhesive microstructure for shear-induced attachment: the effects of pulling angle and preliminary displacement. *J. R. Soc. Interface* **14**: 20170832.
http://dx.doi.org/10.1098/rsif.2017.0832

Received: 6 November 2017
Accepted: 21 November 2017

Subject Category:
Life Sciences–Engineering interface

Subject Areas:
biomimetics

Keywords:
biomimetics, surfaces, tribology, gecko adhesion

Author for correspondence:
Michael Varenberg
e-mail: varenberg@gatech.edu

Electronic supplementary material is available online at https://dx.doi.org/10.6084/m9.figshare.c.3940258.

THE ROYAL SOCIETY PUBLISHING

Biomimetic wall-shaped adhesive microstructure for shear-induced attachment: the effects of pulling angle and preliminary displacement

Jae-Kang Kim and Michael Varenberg

George W. Woodruff School of Mechanical Engineering, Georgia Institute of Technology, Atlanta, GA 30332, USA

MV, 0000-0001-5552-0511

To date, a handful of different gecko-like adhesives inspired by spatula-shaped attachment hairs have been suggested based on wedge and flap geometry of contact elements. However, while these surface designs have been shown to have directionality in adhesion, high friction, long lifetime and the ability to work in vacuum, an experimental verification of the very basic concept of the pulling angle effect has not yet been reported. To close this gap, here we use wall-shaped adhesive microstructures of three different flap heights to systematically study the effect of pulling angle on the normal and tangential components of the pull-off force tested at different preliminary tangential displacements. In accord with the prediction of the Kendall model for the normal component of peeling force, there is an optimal normal force that is required to detach the wall-shaped adhesive microstructure. The optimum is obtained at about half the distance needed to initiate sliding and at pulling angles that range within 60–90°, which suggests that the wall-shaped microstructure can tolerate relatively large inaccuracies in the loading direction. The increase of the attachment force with increasing flap height is found to correlate with the flap thickness, which decreased with increasing flap height.

1. Introduction

Thin-film-ended hairy adhesive structures have evolved independently in insects, arachnids and reptiles to secure their locomotion on substrates of arbitrary orientation, geometry and chemical composition [1]. Since it was revealed that terminal thin-film elements operate using intermolecular [2,3] and, possibly, also capillary [4,5] forces, which allowed these structures to be replicated with engineering materials, much effort has been put into the development of biomimetic adhesive surfaces [6,7]. This led to the introduction of mushroom-shaped microstructures [8,9] mimicking the hairs evolved in male leaf beetles for passive long-term attachment during pairing [10,11]. These microstructures remain the most thoroughly studied to date, perhaps due to the well-established manufacture procedures [9,12,13].

Unlike the mushroom-shaped terminal elements present in male beetles only, a second type of adhesive hairs is based on spatulate geometry, and is characteristic of all hairy attachment pads regardless of the animal group [14]. These spatula-shaped adhesive hairs are known for their ability to be actuated by contact shearing and to be easily released by peeling [15,16], which can make them useful in applications requiring dynamic short-term attachment [17,18]. However, direct replication of these hairs still represents a technological challenge, and careful abstraction and simplification have to be exercised to create an attachment surface mimicking their robust adhesive performance.

To date, a handful of different designs inspired by spatula-shaped adhesive hairs have been suggested based on wedge [19–21] and flap [22–24] geometry of contact elements. These adhesive surface designs were shown to have

© 2017 The Author(s) Published by the Royal Society. All rights reserved.

Downloaded from http://rsif.royalsocietypublishing.org/ on December 19, 2017

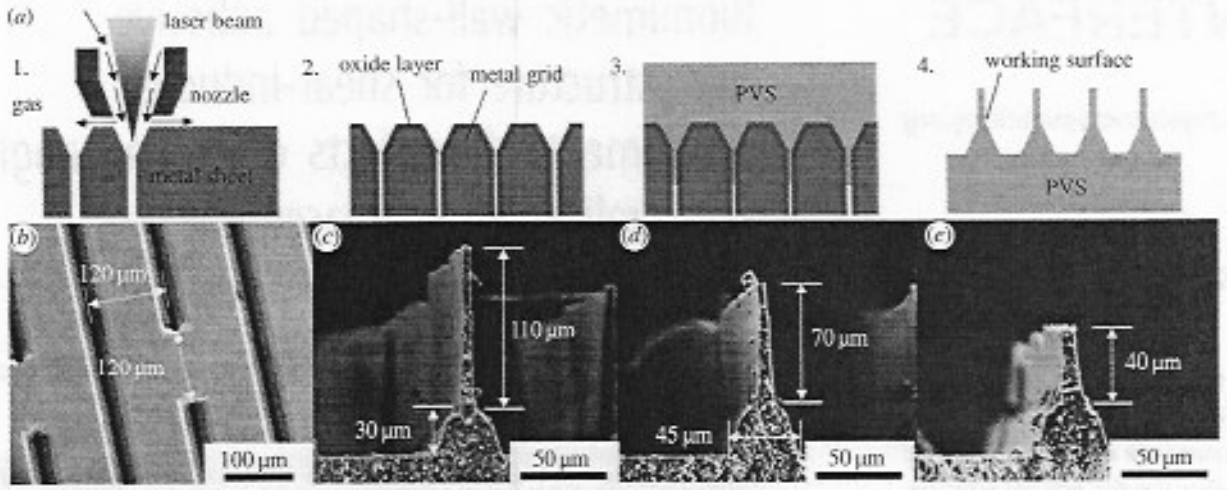


Figure 1. Wall-shaped hierarchic adhesive microstructures. (*a*) Schematic of the fabrication steps. (1) Laser micro-machining, (2) plasma treatment, (3) moulding and (4) release. (*b*) SEM image of the W grid used as a moulding template. (*c–e*) SEM images of single wall-shaped projections with the same triangular bases and different flap heights.

directionality in adhesion [19–23], high friction [20,22,24], effect of tilt [22,23], long lifetime [19,20], sensitivity to substrate roughness [25,26] and ability to work in vacuum [27]. However, an experimental verification of the very basic concept of the pulling angle effect [15,28,29] has not yet been reported. To close this gap, here we use wall-shaped adhesive microstructures [24] of three different flap heights to systematically study the effect of pulling angle on the normal and tangential components of the pull-off force, tested at different preliminary tangential displacements.

2. Material and methods

Microstructured surfaces were moulded from polyvinylsiloxane (PVS, Coltène Whaledent, Altstätten, Switzerland; Young's modulus of about 3 MPa [30]) against a grid of varying cross-section prepared by laser micro-machining (Oxford Lasers, Shirley, MA, USA) from a tungsten sheet of 0.15 mm thickness (figure 1). To facilitate the mould release, which was performed in a water bath, the tungsten grid was oxidized in a PSD-UV4 ozone cleaner (Novascan Technologies, Ames, IA, USA) for 30 min before each moulding. Waiting 100 s, 105 s or 110 s between mixing the two-compound PVS and pouring the polymerizing mixture onto the grid allowed us to create wall-shaped projections of three different heights: 140 µm, 100 µm or 70 µm, respectively. This was possible because the curing PVS stopped sinking into the grid after it reached a certain degree of polymerization at a set time of about 3 min. The dwell times were found experimentally, fitting to $H = 116 \times 10^3 \times 0.935^t$, where H is the height in micrometres and t is the time in seconds. The mould backing layer was made to have a thickness of 1 mm by using spacers between the grid and a flat cover. The PVS was kept at 4°C before mixing and was polymerized during 10 min at room temperature. The mould was gently released from the grid after it was held in a water-filled M1800H ultrasonic bath (Branson Ultrasonics, Danbury, CT, USA) for 30 min.

Samples of 2 mm diameter were cut out of the 1-mm-thick mould using a disposable biopsy Uni-Punch (Premier Products, Plymouth Meeting, PA, USA), so the wall-shaped projections of 800 µm in length had a total peeling line length of 22 mm (on each sample). Then the samples were cleansed with deionized water with soap and dried in blowing nitrogen. A glass slide of 30 × 5 × 1 mm in size and with a roughness average R_a of 5 nm was cleansed with ethanol, deionized water and blowing nitrogen and then used as a counterface. Tested surfaces were inspected with an M125 optical stereomicroscope (Leica, Wetzlar, Germany) and imaged in a Quanta 250 environmental scanning electron microscope (SEM; FEI, Brno, Czech Republic). The SEM was operated in a low-vacuum mode at 130 Pa and 5 kV to enable charge-free imaging of non-conductive samples in their natural state.

The tests were carried out in a custom-built tribometer [31] that enables flat samples to self-align [32] and that can operate inside the SEM. When the tribometer was operated outside the SEM, a monochrome digital camera DMK 23UP1300 (Imaging Source, Charlotte, NC, USA) mounted on a high-magnification optical lens Zoom-12× (Navitar, Rochester, NY, USA) was used to capture images of the real contact area, which was visualized due to the light interference at the glass–PVS interface.

After mounting a structured sample on the tribometer in such a way that the wall-shaped projections were perpendicular to the sliding/pulling direction, the sequence shown in figure 2 was run while recording the generated normal ($F_\perp$) and tangential ($F_\parallel$) forces. First, the glass slide was moved perpendicular to the contact plane until a normal load of 10 mN was achieved. This preload was chosen to be large enough to create good contact and small enough to avoid causing surface damage in sliding. Then, the glass slide was moved in parallel to the contact plane under the same normal load and at a speed of 100 µm s^{-1} for a designated preliminary distance that was changed between 0 and 500 µm. Next, the glass slide was withdrawn from the contact at a speed of 100 µm s^{-1} and at a designated pulling angle φ (figure 2) that was changed between 10° and 170° at intervals of 10°. The test stopped at a complete detachment of the glass slide from the structured sample.

Three samples of each height were tested. The temperature and relative humidity in the laboratory were 25–27°C and 54–55%, respectively.

3. Results and discussions

3.1. Contact forces and characteristic interactions

Several examples of normal ($F_\perp$) and tangential ($F_\parallel$) forces recorded during the tests are shown in figure 3 as a function of tangential displacement. The topmost grey and black curves represent normal and tangential force envelopes obtained during a simple sliding test, in which the normal

Downloaded from http://rsif.royalsocietypublishing.org/ on December 19, 2017

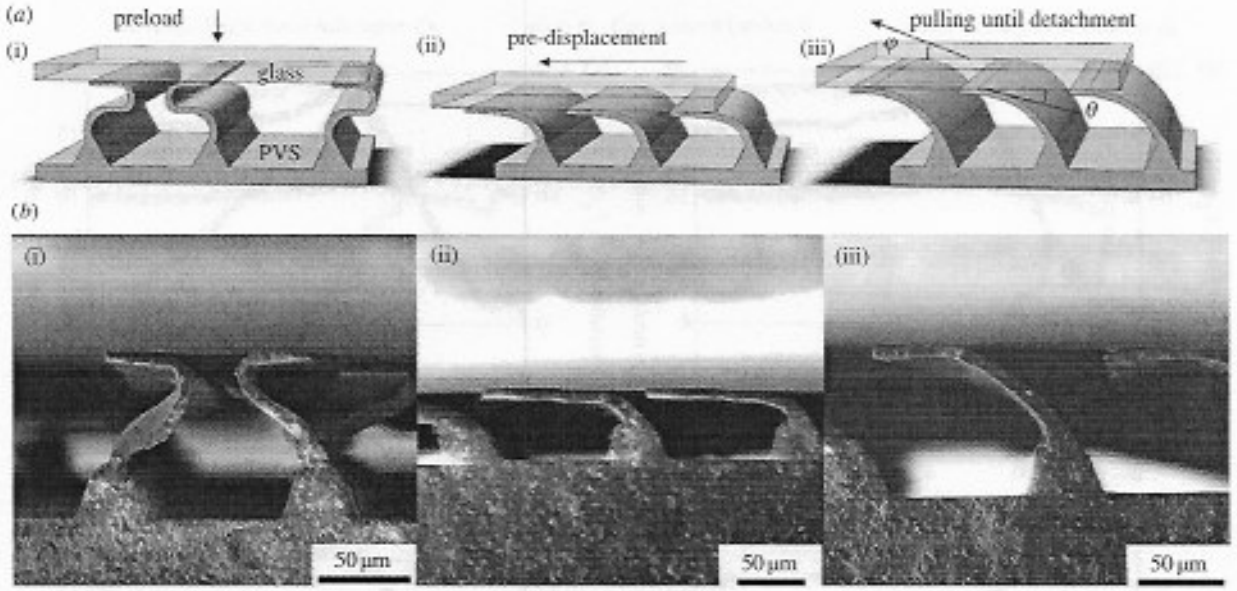


Figure 2. Schematic (*a*) and SEM images (*b*) of the test sequence. (i) Preload is applied. (ii) Pre-displacement is applied while maintaining the same preload. (iii) The glass slide is pulled at a certain pulling angle, φ, while the peeling angle, θ, adjusts itself according to the contact conditions.

force is kept constant, and the tangential force increases until the inception of sliding and then levels off after a small decrease, in a fashion similar to the behaviour of real gecko foot hairs [2]. A sudden drop in the tangential contact stiffness at the initial stage of the sliding test corresponds to the overturning of those wall-shaped projections that initially buckled in the non-preferred direction (figure 2). A decrease in the tangential force after the sliding inception point corresponds to the start of the stick-slip motion of the individual projections, which move asynchronously, leading to a uniform global sliding characterized by average (between static and kinetic) friction [33].

The curves that split from the normal and tangential force envelops in figure 3*a–c* correspond to the forces measured during the withdrawal stage after three characteristic preliminary displacements. The normal force curves look similar in all three cases, with an initial change from compression due to preload to tension due to adhesion, then reaching maximum at the pull-off point, and eventually dropping to zero after the detachment process starts. The tangential force curves have different appearances depending on the preliminary displacement, which allows identification of several modes of contact behaviour.

If withdrawal starts at small preliminary displacement when the wall-shaped projections are not yet aligned and stretched (figure 3*a*), the additional tangential displacement during withdrawal results in more stretching of the projections and a corresponding increase in the tangential force. The tangential force increases until the pull-off point, at which the wall-shaped projections start detaching, resulting in the force decreasing to zero at the point of complete detachment. In this case, some of the surface projections are peeled at very high angles because they are not yet overturned, so their contributions to the total pull-off force are small and the structured surface does not perform at its best.

At intermediate preliminary displacement when the projections are already aligned but are not yet stretched to their maximum ability (figure 3*b*), the additional tangential displacement during withdrawal also results in more stretching and a corresponding increase in the tangential force. However, because the peeling angle θ (figure 2) increases constantly as a result of the flap stretching, the wall-shaped projections start to peel off the counterface before the inception of sliding. While in the peeling mode of operation, the wall-shaped projections seem to obey the prediction of the Kendall model [28], so the tangential force decreases with increasing tensile normal force until the pull-off point, at which the projections start to detach. In this case, the microstructured surface performs at its best and a maximum attachment ability can be expected.

If withdrawal starts after sliding inception (figure 3*c*), the wall-shaped projections are stretched non-uniformly due to their asynchronous stick-slip motion. To this end, they start peeling and pulling off at much more widely distributed tangential displacements. This non-uniformity results in a smaller total pull-off force, leading to a non-optimal overall performance of the microstructured surface.

The curves that split from the normal and tangential force envelopes in figure 3*d–f* correspond to the forces measured during the withdrawal at three characteristic pulling angles. At low pulling angles (figure 3*d*), the microstructured surface starts sliding after a critical tangential displacement is reached, and the stick-slip disturbances undermine the performance of the wall-shaped projections. At high pulling angles (figure 3*f*), the direction of tangential motion is inversed, and the wall-shaped projections are actually unloaded, which also results in a non-optimal performance. At intermediate pulling angles (figure 3*e*), the wall-shaped projections perform at their best, as they are properly loaded, and no detrimental side effects come into force.

The curves shown in figure 3 represent the raw data, from which we extracted several characteristic force values for each combination of the preliminary displacement and the pulling (withdrawal) angle, and for all three types (heights) of the tested surfaces. These force values are the maximum tangential force and the maximum tensile normal (pull-off) force that the microstructured surfaces could generate during each experiment. To analyse the maximum load-carrying capacity, we have also determined the tangential force that corresponds to the pull-off point. The results are discussed below.

Downloaded from http://rsif.royalsocietypublishing.org/ on December 19, 2017

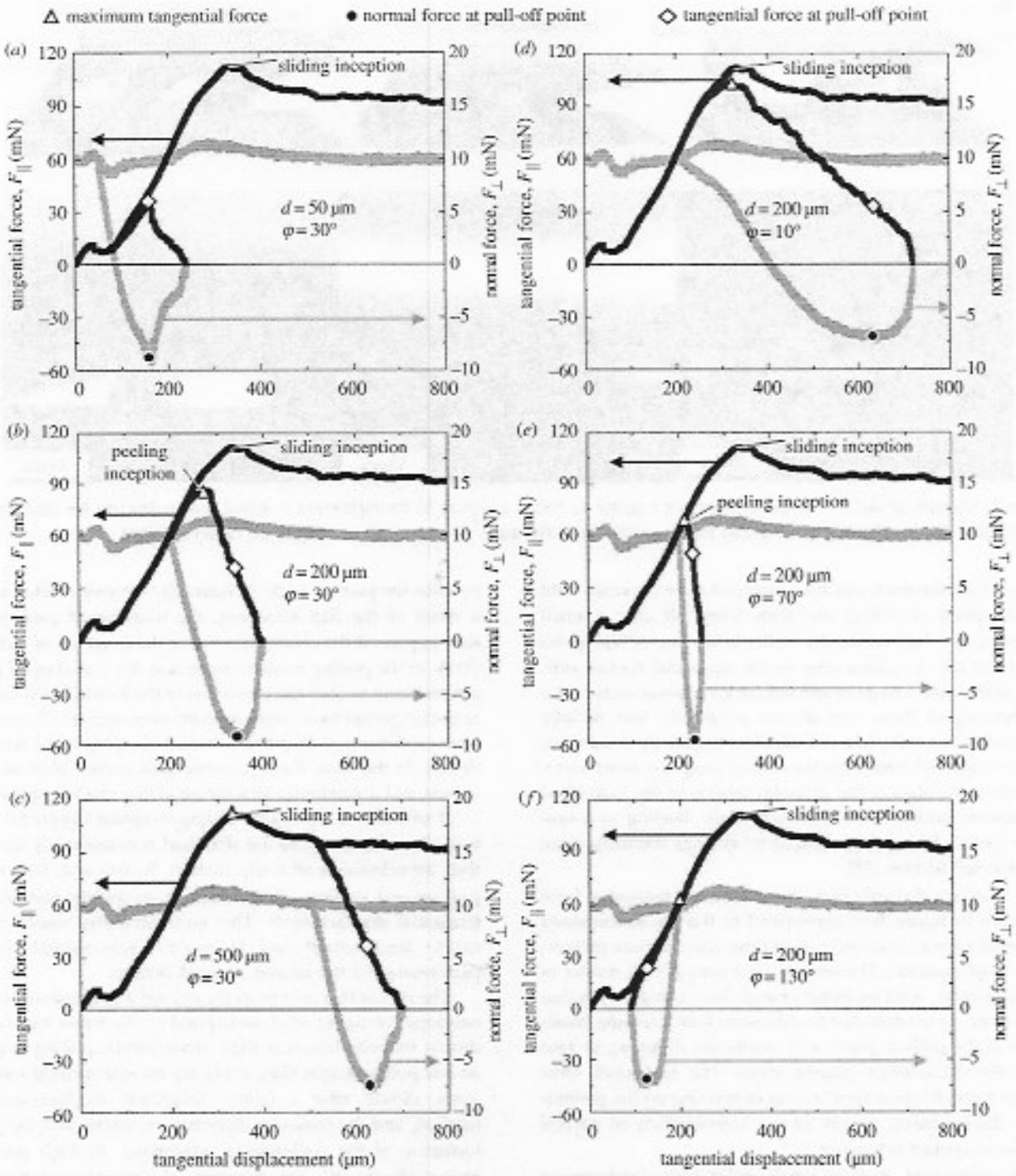


Figure 3. Characteristic examples of normal (in grey) and tangential (in black) forces recorded during the tests. (*a–c*) Preliminary displacement, *d*, of 50, 200, 500 µm, and a pulling angle, *φ*, of 30°. (*d–f*) Preliminary displacement, *d*, of 200 µm, and a pulling angle, *φ*, of 10°, 70°, 130°.

3.2. Effects of preliminary displacement and pulling angle

The maximum tangential ($F_{\parallel}$) force values obtained in different test conditions for three types of the microstructured surfaces are shown in figure 4. As explained above, there are two competing processes that allow for stress relaxation when the surface is loaded—sliding and peeling. When sliding starts first, which happens with smaller preliminary displacements at low pulling angles, and with larger preliminary displacements at high pulling angles, the maximum tangential force is defined by static friction. In this case, the higher the flaps, the larger the real contact area and, hence, the friction. When peeling starts first, which happens with smaller preliminary displacements and higher pulling angles, the maximum tangential force depends on how close the contact is to the verge of the sliding inception. In this case, increasing the preliminary displacement results in increasing the maximum tangential force, and increasing the pulling angle leads to decreasing the maximum tangential force. At pulling angles of more than 90°, as expected, the maximum tangential force depends only on the preliminary displacement. This is because the direction of the tangential motion is inverted in relation to the preliminary displacement, and the microstructured surface is actually unloaded in this direction during withdrawing. Hence, the

Downloaded from http://rsif.royalsocietypublishing.org/ on December 19, 2017

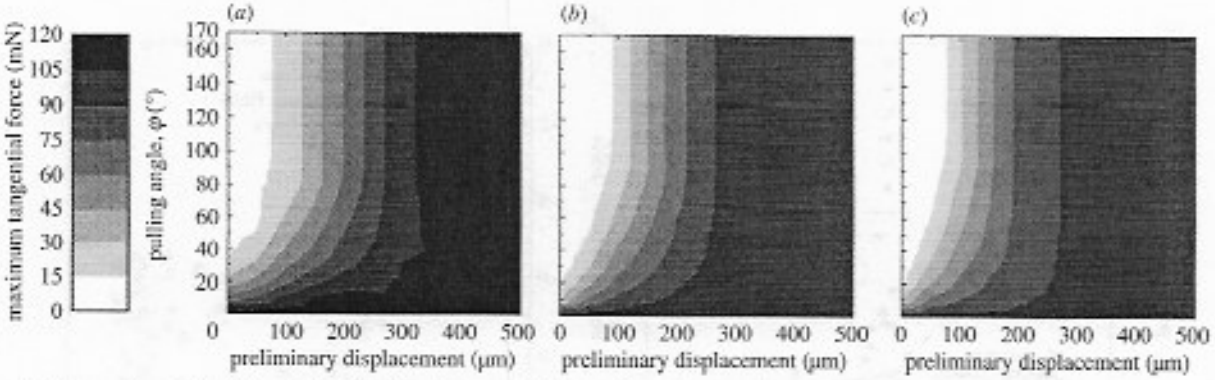


Figure 4. Maximum tangential ($F_{\parallel}$) force obtained under different combinations of preliminary displacements and pulling angle. (*a*) High flaps, (*b*) medium flaps and (*c*) low flaps.

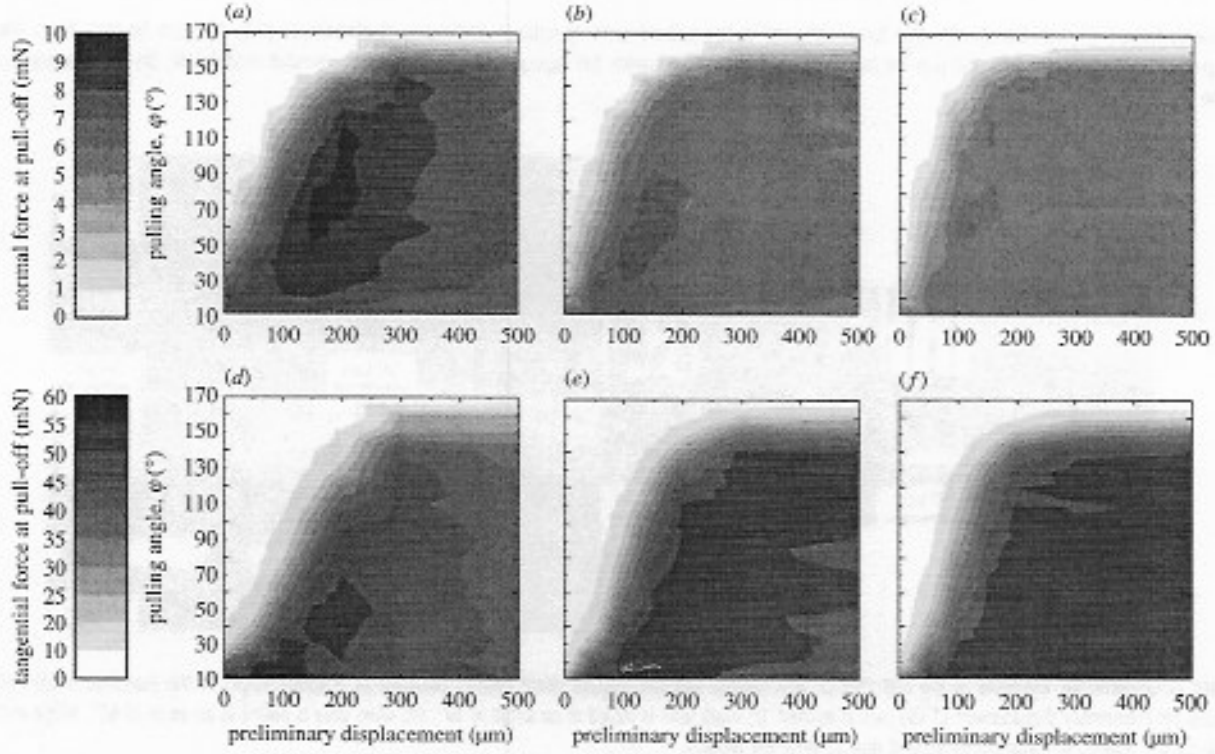


Figure 5. Normal ($F_{\perp}$) and tangential ($F_{\parallel}$) forces obtained at the pull-off point under different combinations of preliminary displacements and pulling angle. (*a*,*d*) High flaps, (*b*,*e*) medium flaps and (*c*,*f*) low flaps.

tangential force decreases with respect to the force generated at the completion of the preliminary displacement.

Figure 5 presents the normal ($F_{\perp}$) and tangential ($F_{\parallel}$) forces obtained at the pull-off point under different combinations of preliminary displacements, pulling angle and flap height. In line with what is expected based on figure 3, the normal (pull-off) force (figure 5*a*–*c*) demonstrates optimum values at the regime of about half the preliminary displacement needed to start sliding (figure 3). At smaller preliminary displacement, the wall-shaped projections are not yet properly aligned after establishing initial contact and random buckling (figure 2). At larger preliminary displacement, the inception of sliding prevents the wall-shaped projections from acting optimally due to a non-uniform tangential load associated with the stick-slip motion.

The withdrawal angles that determine the optimum pull-off force vary within 60–90°, which initially seems to be inconsistent with the previous works, which give a narrow range of optimum peeling angles (e.g. [15,34]). However, this apparent contradiction is resolved if we recall that the withdrawal (pulling) angle does not necessarily correspond to the peeling angle (figure 2). This is because the direction of displacement (input in our case) does not correspond to the direction of force (output in our case) when a slender structure is loaded not in the plane of symmetry [35].

Assuming that the peeling angle should comply with the direction of the peeling force, we can refer to the tangential force map shown in figure 5*d*–*f*. It becomes evident that the region of the optimum normal force coincides well with the contour lines of the tangential force, which gives a constant ratio of the normal over tangential force and results in similar peeling angles for the whole optimum range. This corresponds to the behaviour of real gecko foot hairs, which are known to detach at a narrow range of angles [2,15]. It is worth noting that the wide range of the optimum pulling angles reflects a robustness of the wall-shaped microstructure

Downloaded from http://rsif.royalsocietypublishing.org/ on December 19, 2017

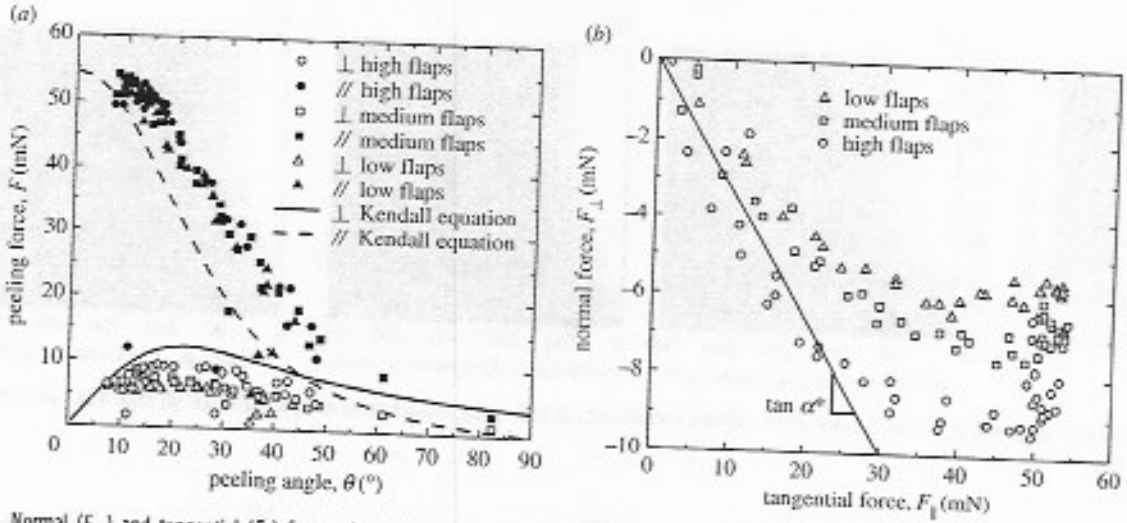


Figure 6. Normal ($F_\perp$) and tangential ($F_\parallel$) forces obtained at the pull-off point at optimal preliminary displacements (150, 200 µm for high flaps; 100, 150, 200 µm for medium flaps; 100, 150 µm for low flaps) and all pulling angles. (*a*) Represented according to the Kendall model [28]. (*b*) Represented according to the Autumn model [15].

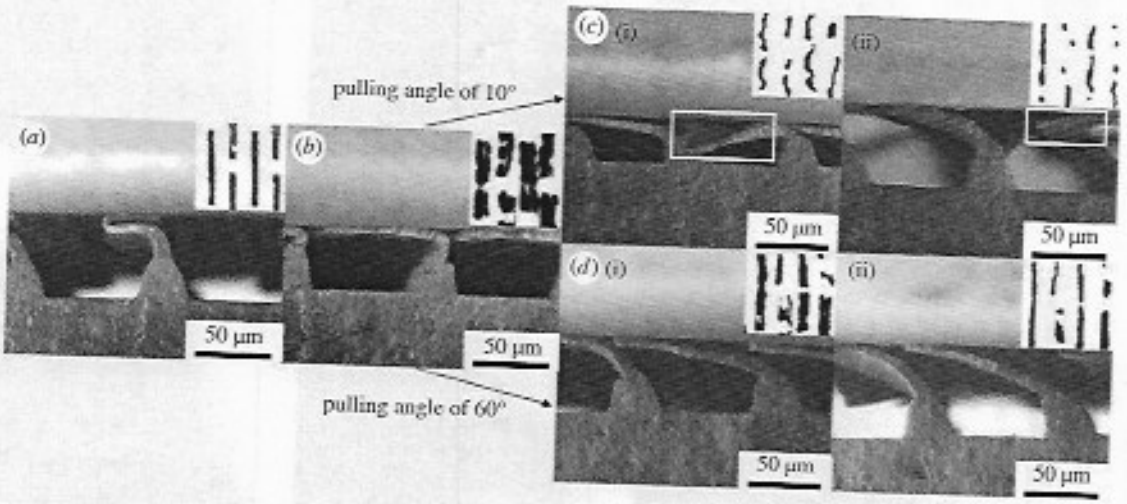


Figure 7. Characteristic examples of the real contact area (insets) and the microstructure profiles obtained at different stages of the experiment. (*a*) Preload is applied. (*b*) Preliminary displacement of 150 µm is applied. (*c*) Glass slide is pulled at an angle of 10°. (*d*) Glass slide is pulled at an angle of 60°. White rectangles highlight the regions of detachment formed due to stick-slip motion.

that can tolerate relatively large inaccuracies in loading direction when in the attachment state and can still detach at zero force when the pulling angles reach 140–160°. This ability to switch between adhesive and non-adhesive states is similar to the performance of real gecko foot hairs [2,15,36], although the critical attachment/detachment angles are different due to differences in the geometries of our artificial attachment structure and the gecko's natural attachment structures.

The difference in the optimum performance of the wall-shaped projections of different heights is not very significant in either the normal and tangential forces, the preliminary displacement or the pulling angles, although all parameters tend to decrease with decreasing height. This can be explained by the fact that shorter flaps both align and start sliding at smaller preliminary displacement, which moves the window of optimum performance towards the origin, which is characterized by lower forces, displacements and angles.

Having the data presented in figure 5, we were also interested to see whether those data are better described using the Kendall model of thin-film peeling [28], or by using the Autumn model stipulating the constant ratio of the normal over the tangential force as an attachment limit [15]. To represent our data correctly, we used only the data subsets corresponding to the optimum preliminary displacements, so neither the initial not-aligned state nor the final stick-slip-affected state of the wall-shaped projections were taken into account. The results are shown in figure 6, where all the force values are measured, and the peeling angles are calculated as $\theta = A \cdot \tan^{-1}(F_\perp/F_\parallel) + B$, where $A = 3, 4.5, 4.5$ and $B = 15, 23, 17$ are the coefficients of the high, medium and low flaps, respectively, adjusted for a better match with the Kendall model. The theoretical normal and tangential components of the model's peeling force were computed based on the equation

$$\left(\frac{F}{b}\right)^2 \frac{1}{2dE} + \frac{F}{b}(1 - \cos\theta) - R = 0, \qquad (3.1)$$

where F is the total peeling force, $b = 22$ mm is the total peeling line length, $d = 6$ µm is the average flap thickness, $E = 3$ MPa is the elastic modulus of the PVS, θ is the peeling angle and $R = 0.17$ N m^{-1} is the fracture energy per unit area

Downloaded from http://rsif.royalsocietypublishing.org/ on December 19, 2017

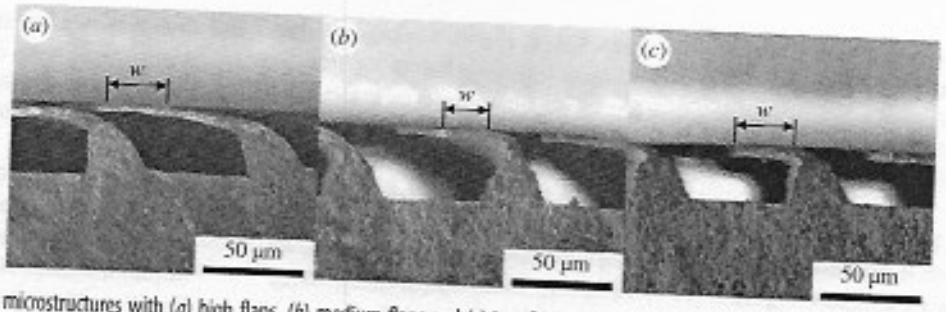


Figure 8. Wall-shaped microstructures with (*a*) high flaps, (*b*) medium flaps and (*c*) low flaps imaged close to the pull-off instability at preliminary displacement of 150 µm and pulling angle of 60°.

chosen to fit the experimental data. The line representing the Autumn model has been drawn based on the best visual fit of the linear portion of the data and has a slope $\tan\alpha^* = 0.33$, which corresponds to a detachment angle α^* of 18°. It is evident that Kendall's approach yields a better fit, while the observed deviations can be associated with the presence of triangular bases and a non-uniform thickness of flaps in the wall-shaped projections. Interestingly, a similar non-linear relationship between the normal and tangential forces (figure 6*b*) is also observed with wedge-shaped gecko-inspired attachment structures [15,21], which throws doubt on the applicability of the Autumn model [15] to current artificial systems. The observed discrepancy may be related to a large difference between the high elastic modulus of the keratinous setae used to devise the Autumn model and the low elastic moduli of the silicon-based elastomers employed in current bioinspired adhesives. This explanation is consistent with Kendall's analysis [28], which can represent the Autumn model as a particular 'no extension' case of a more general solution.

The effects of the preliminary displacement and the pulling angle can also be observed in several characteristic examples of the real contact area and the microstructure profiles demonstrated in figure 7 at different stages of the experiment. When the preload is applied, the wall-shaped projections buckle randomly, resulting in the folded flaps forming a uniform but small contact area (figure 7*a*). Shearing the contact leads to all flaps unfolding and aligning to form a much larger contact area (figure 7*b*) able to carry higher tangential and normal forces. When the tangential displacement is sufficiently large to initiate sliding, stick-slip instabilities lead to random (in time and space) motion of the flaps, so the contact area becomes small and uneven, and as a result the surface cannot support high loads. Such behaviour takes place when the glass counterface is withdrawn at low pulling angles (figure 7*c*). If, however, the pulling angle is sufficiently large to not allow the system to reach the sliding inception (figure 7*d*), the wall-shaped projections peel uniformly and steadily, resulting in the best possible adhesive performance.

It is also interesting to note that, when the point of the pull-off instability is eventually reached, the contact area (peeling line length multiplied by contact width, w) appears to be very similar for the wall-shaped projections of all three heights (figure 8). To this end, because this area is obviously adjacent to the flap edge, the active film is thinner in the higher flaps due to some gradient in thickness, as shown in figure 1. According to the Kendall model, this should result in a higher pull-off force, which is indeed observed for the higher wall-shaped projections tested in our experiments.

4. Conclusion

Testing the wall-shaped adhesive microstructures of three different heights at several preliminary tangential displacements and pulling angles allowed us to draw the following conclusions. In accordance with the prediction of the Kendall model for the normal component of peeling force (figure 6*a*), there is an optimal normal force that is required to detach the wall-shaped adhesive microstructure. The optimum is obtained at about half the distance needed to initiate sliding, as at smaller preliminary displacement the contact flaps are not properly aligned, while at larger preliminary displacements the stick-slip instabilities undermine the uniformity of the load. In terms of the pulling direction, the optimum is obtained within the range of 60–90°, which points to the difference between pulling and peeling angles and suggests that the wall-shaped microstructure can tolerate relatively large inaccuracies in the loading direction. The increase in the attachment force with increasing flap height is found to be weak but measurable and is thought to correlate with the flap thickness, which decreased with increasing flap height.

Data accessibility. The dataset supporting this article has been uploaded as part of the electronic supplementary material.

Authors' contributions. J.-K.K. performed the research, analysed the data and drafted the manuscript. M.V. conceived the research, designed the research and edited the manuscript. All authors gave final approval for publication.

Competing interests. We declare we have no competing interests.

Funding. This work was funded by the Georgia Institute of Technology.

References

1. Scherge M, Gorb S. 2001 *Biological micro- and nanotribology: nature's solutions*. Berlin, Germany: Springer.
2. Autumn K, Liang YA, Hsieh ST, Zesch W, Chan WP, Kenny TW, Fearing R, Full RJ. 2000 Adhesive force of a single gecko foot-hair. *Nature* **405**, 681–685. (doi:10.1038/35015073)
3. Autumn K *et al.* 2002 Evidence for van der Waals adhesion in gecko setae. *Proc. Natl Acad. Sci. USA* **99**, 12 252–12 256. (doi:10.1073/pnas.192252799)
4. Langer MG, Ruppersberg JP, Gorb S. 2004 Adhesion forces measured at the level of a terminal plate of the fly's seta. *Proc. R. Soc. Lond. B* **271**, 2209–2215. (doi:10.1098/rspb.2004.2850)

Downloaded from http://rsif.royalsocietypublishing.org/ on December 19, 2017

5. Huber G, Mantz H, Spolenak R, Mecke K, Jacobs K, Gorb SN, Arzt E. 2005 Evidence for capillarity contributions to gecko adhesion from single spatula nanomechanical measurements. *Proc. Natl Acad. Sci. USA* **102**, 16 293–16 296. (doi:10.1073/pnas.0506328102)
6. Zhou M, Pesika N, Zeng HB, Tian Y, Israelachvili J. 2013 Recent advances in gecko adhesion and friction mechanisms and development of gecko-inspired dry adhesive surfaces. *Friction* **1**, 114–129. (doi:10.1007/s40544-013-0011-5)
7. O'Rorke R, Steele T, Taylor H. 2016 Bioinspired fibrillar adhesives: a review of analytical models and experimental evidence for adhesion enhancement by surface patterns. *J. Adhes. Sci. Technol.* **30**, 362–391. (doi:10.1080/01694243.2015.1101183)
8. Gorb S, Varenberg M, Peressadko A, Tuma J. 2007 Biomimetic mushroom-shaped fibrillar adhesive microstructure. *J. R. Soc. Interface* **4**, 271–275. (doi:10.1098/rsif.2006.0164)
9. Kim S, Sitti M. 2006 Biologically inspired polymer microfibers with spatulate tips as repeatable fibrillar adhesives. *Appl. Phys. Lett.* **89**, 261911. (doi:10.1063/1.2424442)
10. Stork NE. 1980 Experimental analysis of adhesion of *Chrysolina polita* (*Chrysomelidae, Coleoptera*) on a variety of surfaces. *J. Exp. Biol.* **88**, 91–108.
11. Stork NE. 1983 The adherence of beetle tarsal setae to glass. *J. Nat. Hist.* **17**, 583–597. (doi:10.1080/00222938300770481)
12. Murphy MP, Aksak B, Sitti M. 2007 Adhesion and anisotropic friction enhancements of angled heterogeneous micro-fiber arrays with spherical and spatula tips. *J. Adhes. Sci. Technol.* **21**, 1281–1296. (doi:10.1163/156856107782328380)
13. del Campo A, Greiner C, Arzt E. 2007 Contact shape controls adhesion of bioinspired fibrillar surfaces. *Langmuir* **23**, 10 235–10 243. (doi:10.1021/la7010502)
14. Varenberg M, Pugno NM, Gorb SN. 2010 Spatulate structures in biological fibrillar adhesion. *Soft Matter* **6**, 3269–3272. (doi:10.1039/c003207g)
15. Autumn K, Dittmore A, Santos D, Spenko M, Cutkosky M. 2006 Frictional adhesion: a new angle on gecko attachment. *J. Exp. Biol.* **209**, 3569–3579. (doi:10.1242/jeb.02486)
16. Tian Y, Pesika N, Zeng HB, Rosenberg K, Zhao BX, McGuiggan P, Autumn K, Israelachvili J. 2006 Adhesion and friction in gecko toe attachment and detachment. *Proc. Natl Acad. Sci. USA* **103**, 19 320–19 325. (doi:10.1073/pnas.0608841103)
17. Daltorio KA, Gorb S, Peressadko A, Horchler AD, Ritzmann RE, Quinn RD. 2006 A robot that climbs walls using micro-structured polymer feet. In *Climbing and walking robots* (eds MO Tokhi, GS Virk, MA Hossain), pp. 131–138. Berlin, Germany: Springer.
18. Menguc Y, Yang SY, Kim S, Rogers JA, Sitti M. 2012 Gecko-inspired controllable adhesive structures applied to micromanipulation. *Adv. Funct. Mater.* **22**, 1246–1254. (doi:10.1002/adfm.201101783)
19. Parness A, Soto D, Esparza N, Gravish N, Wilkinson M, Autumn K, Cutkosky M. 2009 A microfabricated wedge-shaped adhesive array displaying gecko-like dynamic adhesion, directionality and long lifetime. *J. R. Soc. Interface* **6**, 1223–1232. (doi:10.1098/rsif.2009.0048)
20. Chary S, Tamelier J, Turner K. 2013 A microfabricated gecko-inspired controllable and reusable dry adhesive. *Smart Mater. Struct.* **22**, 025013. (doi:10.1088/0964-1726/22/2/025013)
21. Day P, Eason EV, Esparza N, Christensen D, Cutkosky M. 2013 Microwedge machining for the manufacture of directional dry adhesives. *J. Micro Nano-Manuf.* **1**, 011 001–011 010. (doi:10.1115/1.4023161)
22. Yu J, Chary S, Das S, Tamelier J, Pesika NS, Turner KL, Israelachvili JN. 2011 Gecko-inspired dry adhesive for robotic applications. *Adv. Funct. Mater.* **21**, 3010–3018. (doi:10.1002/adfm.201100493)
23. Jin K, Tian Y, Erickson JS, Puthoff J, Autumn K, Pesika NS. 2012 Design and fabrication of gecko-inspired adhesives. *Langmuir* **28**, 5737–5742. (doi:10.1021/la204040p)
24. Kasem H, Tsipenyuk A, Varenberg M. 2015 Biomimetic wall-shaped hierarchical microstructure for gecko-like attachment. *Soft Matter* **11**, 2909–2915. (doi:10.1039/C4SM01916D)
25. Yu J, Chary S, Das S, Tamelier J, Turner KL, Israelachvili JN. 2012 Friction and adhesion of gecko-inspired PDMS flaps on rough surfaces. *Langmuir* **28**, 11 527–11 534. (doi:10.1021/la301783q)
26. Kasem H, Cohen Y. 2017 Effect of counterface roughness on the friction of bionic wall-shaped microstructures for gecko-like attachments. *Bioinspir. Biomim.* **12**, 046010. (doi:10.1088/1748-3190/aa7720)
27. Tao DS, Gao X, Lu HY, Liu ZY, Li Y, Tong H, Pesika N, Meng YG, Tian Y. 2017 Controllable anisotropic dry adhesion in vacuum: gecko inspired wedged surface fabricated with ultraprecision diamond cutting. *Adv. Funct. Mater.* **27**, 1606576. (doi:10.1002/adfm.201606576)
28. Kendall K. 1975 Thin-film peeling—elastic term. *J. Phys. D Appl. Phys.* **8**, 1449–1452. (doi:10.1088/0022-3727/8/13/005)
29. Pesika NS, Tian Y, Zhao BX, Rosenberg K, Zeng HB, McGuiggan P, Autumn K, Israelachvili JN. 2007 Peel-zone model of tape peeling based on the gecko adhesive system. *J. Adhesion* **83**, 383–401. (doi:10.1080/00218460701282539)
30. Peressadko A, Gorb SN. 2004 When less is more: experimental evidence for tenacity enhancement by division of contact area. *J. Adhesion* **80**, 247–261. (doi:10.1080/00218460490430199)
31. Murarash B, Varenberg M. 2011 Tribometer for in situ scanning electron microscopy of microstructured contacts. *Tribol. Lett.* **41**, 319–323. (doi:10.1007/s11249-010-9717-y)
32. Varenberg M, Peressadko A, Gorb S, Arzt E. 2006 Effect of real contact geometry on adhesion. *Appl. Phys. Lett.* **89**, 121905. (doi:10.1063/1.2356099)
33. Kligerman Y, Varenberg M. 2014 Elimination of stick-slip motion in sliding of split or rough surface. *Tribol. Lett.* **53**, 395–399. (doi:10.1007/s11249-013-0278-8)
34. Heepe L, Raguseo S, Gorb SN. 2017 An experimental study of double-peeling mechanism inspired by biological adhesive systems. *Appl. Phys. A* **123**, 124. (doi:10.1007/s00339-016-0753-9)
35. Timoshenko S. 1976 *Strength of materials*, 3rd edn. Huntington, NY: R. E. Krieger Pub. Co.
36. Zhao BX, Pesika N, Rosenberg K, Tian Y, Zeng HB, McGuiggan P, Autumn K, Israelachvili J. 2008 Adhesion and friction force coupling of gecko setal arrays: implications for structured adhesive surfaces. *Langmuir* **24**, 1517–1524. (doi:10.1021/la702126k)